Domain Decomposition and Model Order Reduction for Electromagnetic Field Simulations in Carbon Fiber Composite Materials

Suyang Lou, Antoine Pierquin, Guillaume Wasselynck, Didier Trichet, Nicolas Bracikowski

applied sciences

MDPI

Article

Domain Decomposition and Model Order Reduction for Electromagnetic Field Simulations in Carbon Fiber Composite Materials

Suyang Lou *, Antoine Pierquin, Guillaume Wasselynck, Didier Trichet and Nicolas Bracikowski

Institut de Recherche en Énergie Électrique de Nantes Atlantique, IREENA, Nantes Universite, UR 4642, F-44600 Saint-Nazaire, France; antoine.pierquin@univ-nantes.fr (A.P.); guillaume.wasselynck@univ-nantes.fr (G.W.); didier.trichet@univ-nantes.fr (D.T.); nicolas.bracikowski@univ-nantes.fr (N.B.)

* Correspondence: suyang.lou@gmail.com

Featured Application: Carbon-fibre-reinforced Polymer (CFRP) is a widely used material in the aerospace industry, but the flaws inside are difficult to detect and may be the cause of failure. This study investigates the simulation of flaw detection at the fibre scale in CFRP using induction thermography to validate the accuracy of this detection. Given the extensive number of unknowns involved in such simulations, one proposes a novel order reduction method combining proper orthogonal decomposition and domain decomposition. Numerical results demonstrate that this approach significantly reduces solution time while maintaining precision.

Abstract: The computation of the electric field in composite materials at the microscopic scale results in an immense number of degrees of freedom. Consequently, this often leads to prohibitively long computation times and extensive memory requirements, making direct computation impractical. In this study, one employs an innovative approach that integrates domain decomposition and model order reduction to retain local information while significantly reducing computation time. Domain decomposition allows for the division of the computational domain into smaller, more manageable subdomains, enabling parallel processing and reducing the overall complexity of the problem. Model order reduction further enhances this by approximating the solution in a lower-dimensional subspace, thereby minimising the number of unknown variables that need to be computed. Comparative analysis between the results obtained from the reduced model and those from direct resolution demonstrates that our method not only reduces computation time but also maintains accuracy. The new method effectively captures the essential characteristics of the electric field distribution in composite materials, ensuring that the local phenomena are accurately represented. This study provides a contribution to the field of computational electromagnetics by presenting a feasible solution to the challenges posed by the high computational demands of simulating composite materials at the microscopic scale. The proposed methodology offers a promising direction for future research and practical applications, enabling more efficient and accurate simulations of complex material systems.

Keywords: model order reduction (MOR); domain decomposition (DD); multi-scale simulation

Citation: Lou, S.; Pierquin, A.; Wasselynck, G.; Trichet, D.; Bracikowski, N. Domain Decomposition and Model Order Reduction for Electromagnetic Field Simulations. *Appl. Sci.* **2024**, *14*, 6013. https://doi.org/10.3390/app14146013

Academic Editors: Piotr Gas, Gang Li, Chuandong Jiang and Haigen Zhou

Received: 16 May 2024
Revised: 4 July 2024
Accepted: 8 July 2024
Published: 10 July 2024

1. Introduction

Carbon-fibre-reinforced polymers (CFRPs) are fibre-reinforced plastics that consist of carbon fibres separated by resin. Due to its great mechanical characteristics and lightness, CFRPs have developed rapidly and became the main material in the aerospace industry [1,2]. A CFRP is a pile up of several unidirectional layers. In each layer, the carbon fibres are not straight but they are oriented in the same direction, and the fibres are randomly arranged in the cross section. The orientation of fibres in each layer is set according

to the future mechanical solicitations of the pile up. Composites are highly anisotropic and heterogeneous, especially from an electrical point of view.

Flaws may occur within these materials with complex structures and are difficult to detect, including voids, delamination, fibre misalignments, and matrix cracks [3,4]. These flaws can significantly impact the material's performance and integrity. For example, voids can affect the level of strength and elasticity; delamination can lead to a drastic reduction in load-bearing capacity; fibre misalignments can weaken the composite structure; and matrix cracks can initiate and propagate under stress, leading to a gradual deterioration of mechanical properties.

In order to carry out the inspection on composites and guarantee their integrity, Non-Destructive Testing (NDT) is commonly used. Among them, induction thermography (Figure 1) is a testing method where the eddy currents in the material to inspect, induced by an external variable magnetic source, are disturbed by the presence of an internal flaw. The resulting heat flow is then also disturbed, which causes an abnormal temperature variation at the surface of the material. The latter can be detected by an infrared camera and correlated to the internal defect [5–7].

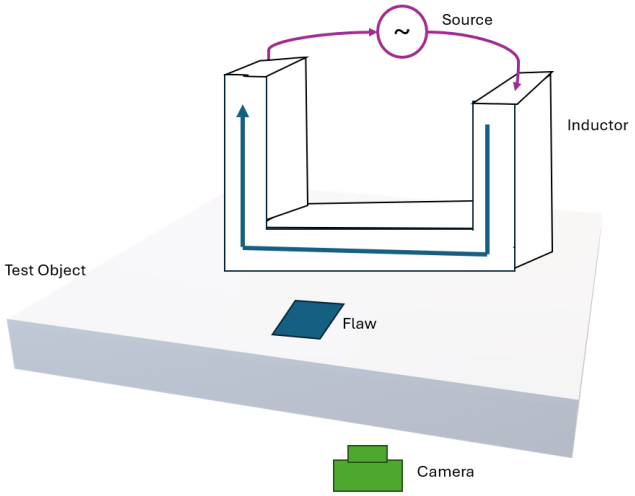

Figure 1. General operating principles of induction thermography [8].

Numerical simulation of such a material is useful to understand and predict its behaviour but can be complicated. To deal with composite materials, there are three scales to study (Figure 2): the microscopic scale (fibre scale, micrometres), the mesoscopic scale (layers scale, hundreds of micrometres), and the macroscopic scale (structure scale, several metres). Due to the huge ratio between microscopic and macroscopic scales, direct simulation at both scales at the same time is impossible because it would generate numerous unknowns, resulting in a long computation time and high computational resources.

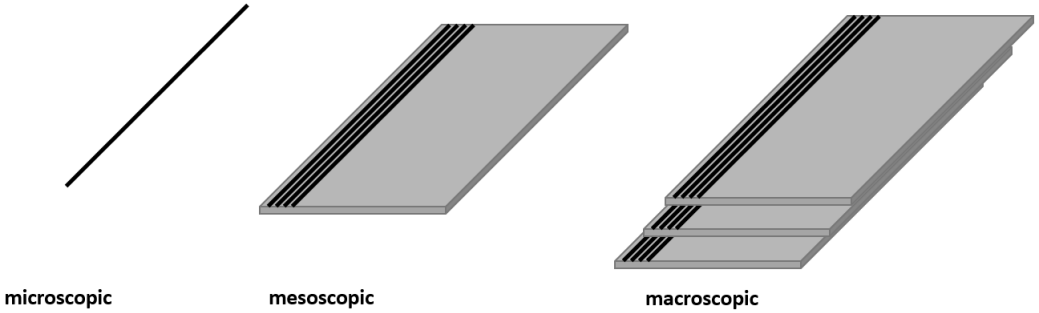

Figure 2. Three scales of composite materials: microscopic, mesoscopic, and macroscopic.

In previous work, the equivalent circuit approach is used to model the electrical behaviour of CFRP at a microscopic scale. The equivalent circuit approach has the advantage of eliminating the 3D mesh of the fibres, in particular by considering electrical resistance to represent

the fibres and the contacts between them, thus preserving spatial localisation and interactions between the fibres at the microscopic scale [9–11]. However, the simulation of a composite using an equivalent circuit approach always generates a high number of degrees of freedom in order to achieve a realistic size of the material; then, homogenisation methods are used to make the transition from the microscopic to the mesoscopic scale [10,12]. During the homogenisation process, local information may be lost. To overcome this problem, the Domain Decomposition method (DD) and/or Model Order Reduction methods (MOR) methods can be applied.

In the context of large domain simulation, DD is usually used to decompose the computation into several sub-domains [13]; then, parallel computing can be applied. On other hand, MOR methods such as Proper Generalised Decomposition (PGD) [14,15] or Proper Orthogonal Decomposition (POD) [16–19] can effectively reduce the computational complexity. The idea of PGD is to decompose the solution into a sum of the product of functions with independent variables and solve the equation for each variable iteratively. PGD is suitable for the finite element formulation but is less suitable for a circuit formulation with a discontinuous domain as PGD presents difficulty in separating the resolution in the fibre direction and the layer: it is undeniable that PGD is an effective method for dimensionality reduction and can be coupled with domain decomposition in several recent studies [20,21]; however, for our materials and the specific requirements of circuit formulation with a discontinuous domain on each node of local fibres, as the position of the fibres in each plane is inherently linked to their position along the fibre direction, the interdependency makes it challenging to completely decouple the spatial variables in all three directions during the solution process, which is a fundamental requirement for PGD. The idea of POD is to project the resolution from a complete space to a reduced subspace. This paper presents the methodology of DD with POD on CFRP to simulate an induction control process while conserving information at the microscopic scale.

The precedent work on the combination of DD and POD uses POD to speed up the resolution by DD in each subdomain, which means that POD is applied in each subdomain [22,23] and POD usually works on time-based variables. In our context, POD will be used on geometric parameters on the global domain: POD can project the relation of the global domain into subdomains, which speeds up the convergence of DD. The details will be presented in the following sections.

2. Problem Statement

A domain is divided into several small cells, with each cell being a set of carbon fibres generated by an algorithm, allowing us to obtain a virtual material with properties close to the real ones (Figure 3) [12].

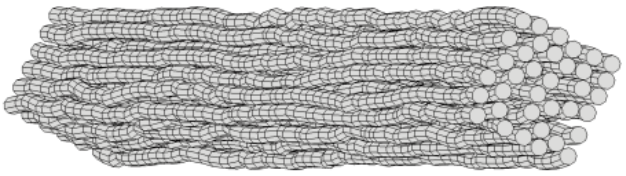

Figure 3. An example of virtual material with the same microscopic behaviour as real material.

The fibres stretch in the z direction and are randomly distributed in x and y directions in the real material. Due to the random positions of the fibres in the composite material, contact between fibres is also possible and random. The presence of contacts has a major impact on the induced current because the contact allows the current to pass from one fibre to another. To explain the electrical conductive behaviour of composite materials made up of conductive charges and insulating matrices, percolation theory can be applied. As the conductive charges increases, the composite undergoes a transition from insulator to conductor. The percolation threshold is reached when the measured electrical conductivity of the composite material jumps. Below the percolation threshold, electrical paths do not exist and electrical properties are dominated by the material matrix. The concentration

of conductive charge must be higher than the percolation threshold in order to obtain conductive networks [24].

In the virtual material, when one generates fibres, fibres are divided into layers, and nodes are defined as the centre of fibres at each layer. Nodes are randomly distributed into the layer but with the constraint of limited overlapping between fibres. The layers are built sequentially, with the position of a node in a layer being obtained by the perturbation of the node of the same fibre in the previous layer. A resistance network will be deduced from fibres' geometry and contact between them, as shown in Figure 4.

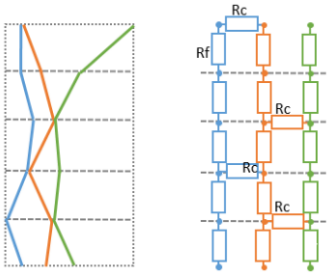

Figure 4. Equivalent resistance network deduced from fibres' geometry.

To simulate the electrical behaviour of CFRP, a global model is given by the following equation:

$$\mathbf{J} = -\sigma \nabla V - \sigma j \omega \mathbf{A}, \tag{1}$$

where $\mathbf{J}$ is the density of current, σ is the conductivity of the carbon, V is the electric potential to be solved, j is the imaginary unit, ω is angular frequency, and $\mathbf{A}$ is the magnetic potential vector.

This model is obtained from

$$\mathbf{E} = -\frac{\partial \mathbf{A}}{\partial t} - \nabla V, \tag{2}$$

$$\mathbf{J} = \sigma \mathbf{E} \tag{3}$$

with

$$\mathbf{B} = \mathrm{rot}\mathbf{A}; \tag{4}$$

where $\mathbf{E}$ is the electric field, $\mathbf{B}$ is the magnetic induction as a source term, and t is the time.

From the Equation (1), one has

$$\frac{\mathbf{J}}{\sigma} = -\nabla V - j\omega \mathbf{A}. \tag{5}$$

When there exists contact between two nodes, the segment connecting them is defined as edge ℓ. From the volume integral on a volume $\ell \times S$ of Equation (5), one has

$$\int_\ell \iint_S \frac{\mathbf{J}}{\sigma} \mathrm{d}S\mathrm{d}\ell = -j\omega \int_\ell \iint_S \mathbf{A}\mathrm{d}S\mathrm{d}\ell - \int_\ell \iint_S \nabla V \mathrm{d}S\mathrm{d}\ell, \tag{6}$$

where S is the cross-sectional area of a fibre.

Then,

$$\begin{aligned} \frac{I\ell}{\sigma} &= -j\omega S \int_\ell \mathbf{A} \cdot \mathrm{d}\ell + S\Delta V, \\ \frac{I\ell}{S\sigma} &= -j\omega \int_\ell \mathbf{A} \cdot \mathrm{d}\ell + \Delta V, \\ IR &= -j\omega \int_\ell \mathbf{A} \cdot \mathrm{d}\ell + \Delta V, \end{aligned} \tag{7}$$

where R is the resistance of segment. In the direction of fibre, the resistance of fibre R_c is added between nodes; in cross-sectional, when the distance between two nodes is less than the diameter of fibre, the resistance of contact is added between these nodes, as shown in Figure 4.

Then, the current is written as

$$I = -\frac{j\omega}{R}\int_{\ell}\mathbf{A}\cdot \mathrm{d}\ell + \frac{\Delta V}{R}. \tag{8}$$

One defines $\mathbf{G}V$ to represent the differentiation operator ΔV and c_A to represent the circulation of $j\omega\mathbf{A}$ on the edge between nodes; then, one introduces the diagonal matrix of conductance $\mathbf{C}$ and has

$$\mathbf{CG}V \triangleq \frac{\Delta V}{R}, \quad \mathbf{C}c_A \triangleq -\frac{j\omega}{R}\int_{\ell}\mathbf{A}\cdot \mathrm{d}\ell. \tag{9}$$

The matrix $\mathbf{D}$ is defined to represent the discrete divergence operator. Applying divergence $\mathbf{D}$ on Equation (8) to impose div$\mathbf{J} = 0$, one has

$$\mathbf{DCG}V = -\mathbf{D}c_A \tag{10}$$

One defines $\mathbf{K} = \mathbf{DCG}$ and $f = -\mathbf{D}c_A$.

The global linear system obtained is written as

$$\mathbf{K}V = f, \tag{11}$$

For a material divided into $2 \times 2 \times 2$ cells, as shown in Figure 5, the system (11) can be rewritten in matrix form:

$$\underbrace{\begin{bmatrix} \mathbf{K}_{11} & \mathbf{K}_{12} & \mathbf{K}_{13} & \mathbf{K}_{14} & \mathbf{K}_{15} & & & \\ \mathbf{K}_{21} & \mathbf{K}_{22} & \mathbf{K}_{23} & \mathbf{K}_{24} & & \mathbf{K}_{26} & & \\ \mathbf{K}_{31} & \mathbf{K}_{32} & \mathbf{K}_{33} & \mathbf{K}_{34} & & & \mathbf{K}_{37} & \\ \mathbf{K}_{41} & \mathbf{K}_{42} & \mathbf{K}_{43} & \mathbf{K}_{44} & & & & \mathbf{K}_{48} \\ \mathbf{K}_{51} & & & & \mathbf{K}_{55} & \mathbf{K}_{56} & \mathbf{K}_{57} & \mathbf{K}_{58} \\ & \mathbf{K}_{62} & & & \mathbf{K}_{65} & \mathbf{K}_{66} & \mathbf{K}_{67} & \mathbf{K}_{68} \\ & & \mathbf{K}_{73} & & \mathbf{K}_{75} & \mathbf{K}_{76} & \mathbf{K}_{77} & \mathbf{K}_{78} \\ & & & \mathbf{K}_{84} & \mathbf{K}_{85} & \mathbf{K}_{86} & \mathbf{K}_{87} & \mathbf{K}_{88} \end{bmatrix}}_{\mathbf{K}} \underbrace{\begin{bmatrix} V_1 \\ V_2 \\ V_3 \\ V_4 \\ V_5 \\ V_6 \\ V_7 \\ V_8 \end{bmatrix}}_{V} = \underbrace{\begin{bmatrix} f_1 \\ f_2 \\ f_3 \\ f_4 \\ f_5 \\ f_6 \\ f_7 \\ f_8 \end{bmatrix}}_{f}. \tag{12}$$

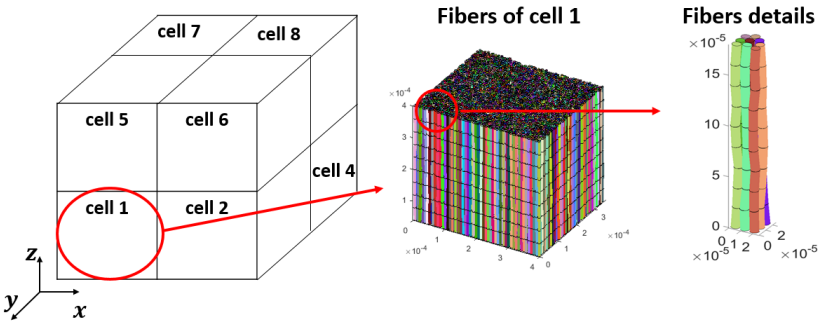

Figure 5. The construction of material for $2 \times 2 \times 2$ case.

V_i is the matrix of potential and f_i is the source for cell i. The diagonal matrices $\mathbf{K}_{ii}$ are the matrix **DCG** defined in the cell plus the contributions of the nodes in contact with neighbouring cells added on the matrix of conductance C in the cell i; the matrices $\mathbf{K}_{ij}$, $i \neq j$, contain the contributions of the nodes of the cell j in contact with the cell i. Due to the division of material shown in Figure 5, except for $\mathbf{K}_{ij}$ and $\mathbf{K}_{ii}$ listed in Equation (12), other cells are not adjacent and their corresponding matrices of conductance are 0. The di-

rect solution may be costly in terms of calculation time because the number of unknowns is too large; therefore, DD and POD are introduced.

3. Domain Decomposition and Application

3.1. Domain Decomposition

The main idea of DD is to decompose a domain into subdomains with small covering and use the obtained solutions on neighbouring contact nodes as boundary conditions for the domain that one is considering [25], as shown in Figure 6.

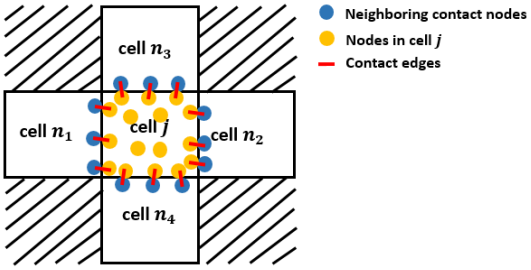

Figure 6. The application of DD for traverse case.

For initialisation, the system in each cell is written as

$$\mathbf{K}_j V_j = f_j, \tag{13}$$

where $\mathbf{K}_j$ is the matrix **DCG** in the cell j without adding the contributions of the nodes in contact with neighbouring cells.

In order to take into account the current between cells, after initialisation, the contact nodes in neighbouring cells are considered in the new system. For cell j, its neighbouring cells are denoted as cell n_1, cell n_2, cell n_3, cell n_4, cell n_5, and cell n_6. The new system in cell j is written as

$$\mathbf{K}_{jj} V_j + \mathbf{K}_{jn_1} V_{n_1} + \mathbf{K}_{jn_2} V_{n_2} + \ldots \mathbf{K}_{jn_6} V_{n_6} = f_j. \tag{14}$$

where $\mathbf{K}_{jj}$ and $\mathbf{K}_{jn_i}$ have the same definition as in the Equation (12).

In DD solving, the system (14) will be solved plenty of times until convergence. The values in neighbouring cells are imposed by the solution obtained in the previous iteration. Therefore, for iteration i, system (14) can be rewritten as

$$\mathbf{K}_{jj} V_j^i = f_j - (\mathbf{K}_{jn_1} V_{n_1}^{i-1} + \mathbf{K}_{jn_2} V_{n_2}^{i-1} + \ldots \mathbf{K}_{jn_6} V_{n_6}^{i-1}). \tag{15}$$

If the covering between subdomains increase, DD converges faster [26]; however, the covering argument increases the number of unknowns. For our case, it is difficult to define a larger covering than adjacent nodes due to the random position of fibres in cross-section. In this paper, model order reduction is coupled to domain decomposition to artificially increase the overlapping without a complex algorithm to search fibres, which are in adjacent subdomains. Indeed, the POD allows for projecting the influence of global nodes onto adjacent nodes. In the next part, the coupling between DD and POD is shown.

3.2. Domain Decomposition with Proper Orthogonal Decomposition

The idea of POD is to extract a basis matrix from a matrix of *snapshots* and reduce the global system by a projection on the basis [27]. In this article, the matrix of *snapshots* is chosen as the solutions in each cell and the basis function is obtained by singular value decomposition on the matrix of *snapshots*

The reduced system is defined as

$$M^t \mathbf{K} M v_r = M^t f, \tag{16}$$

with the basis matrix M on our example defined by

$$M = \begin{bmatrix} M_1 & & & \\ & M_2 & & \\ & & \ddots & \\ & & & M_8 \end{bmatrix}, \tag{17}$$

where the reduced basis M_j for the cell j is obtained by singular value decomposition on the matrix of *snapshots* S_j in the cell j. Let $S_j = U\Sigma W^t$; then, M_j is made of first columns of U and the number of columns of M_j is chosen based on energetic singular values criterion [28].

To initialise the matrix of *snapshots*, one solves the equation without magnetic source imposed:

$$\mathbf{K}_j V_j = 0, \tag{18}$$

with Dirichlet conditions imposed in x, y, and z boundaries in each cell j, which means the input and output voltage are imposed on the boundary of cell in x, y, and z directions, and obtains the solution V_j^x, V_j^y, and V_j^z.

For each cell, the matrix of *snapshots* S_j is initialised as

$$S_j = \left[\mathbf{1}, V_j^x, V_j^y, V_j^z\right], \quad \text{with} \quad \mathbf{1} = \left[1, 1, \ldots, 1\right]^t. \tag{19}$$

The constant vector allows a translation of the solution in each cell. It is not essential, but it gives a better initialisation.

The solution V_{POD} projected in the material is calculated as

$$V_{\mathrm{POD}} = M v_r. \tag{20}$$

Then, the system (21) is repeated in each cell until the convergence with the potential obtained by POD in the precedent iteration is imposed on contact nodes in neighbouring cells.

$$\mathbf{K}_{jj} V_j^i = f_j - (\mathbf{K}_{jn_1} V_{POD}^{i-1} + \mathbf{K}_{jn_2} V_{POD}^{i-1} + \cdots + \mathbf{K}_{jn_6} V_{POD}^{i-1}). \tag{21}$$

Further, the matrix of *snapshots* in each cell is uploaded with the solution obtained by system (21) as

$$S_j^i = [S_j^{i-1}, V_j^i]. \tag{22}$$

Then, the basis M is uploaded and the reduced system (16) is uploaded to obtain the new potential V_{POD} for the next iteration.

To summarise, the algorithm of DD-POD is as follows:

1. Initialisation: initialise the matrix of *snapshots* as Equations (18) and (19).
2. Iterative resolution:
   - Solve the reduced system as Equation (16) and project reduced solution on full domain with (20);
   - Solve Equation (21) in each cell with the solution on full domain by POD imposed and update the matrix of *snapshots* as Equation (22).
3. Repeat the second step until convergence.

4. Numerical Results

The simulation is carried on material of size 800 µm × 800 µm × 800 µm. The radius of the fibre is 3.5 µm. The material is divided into 2 × 2 × 2 cells. Therefore, the size of cell is 400 µm × 400 µm × 400 µm. Every cell has 2500 fibres and each fibre is divided into

10 layers; one cell has 25,000 nodes, and the material has 200,000 nodes. The system (11) has 200,000 unknowns to be solved.

The resistance of fibre is 17.92 Ω, which is calculated by $R_f = \frac{\mathrm{d}z}{\sigma \pi r^2}$ with the distance between two plies dz = 40 µm, the conductivity of carbon $\sigma = 58 \times 10^3$ S m, and the radius of the fibre r = 3.5 µm [11]. The resistance of contact is 11 Ω, which is defined by an analytical model based on Hertz contact theory and Holm's formula [10].

4.1. Error Estimation

For the simulation of induction thermography NDT, current and power estimation is important. According to our model, the potential has been solved, the current can be calculated according to Equation (8), and the power is defined as the power generated by the eddy current that can be calculated according to the current and resistance. In order to verify the accuracy, one should compare the potential and current obtained by the new method and those obtained directly by the global system (11).

The relative error is defined as

$$\mathrm{err}_S = \frac{\|S_{\mathrm{new}} - S\|}{\|S\|}, \tag{23}$$

where S_{new} is the solution being the potential V, the current I and the power M are solved by the new method (DD or DD-POD), and S is the reference solution directly solved by the global system.

Firstly, the comparison of convergence is performed between DD and DD-POD. The imposed magnetic source is the magnetic field $\mathbf{B}$ along the x, y, and z directions, noted as $\mathbf{B}_x$, $\mathbf{B}_y$, and $\mathbf{B}_z$. In order to compare the convergence without penalising DD with a bad initialisation, one uses the first solution of DD-POD from the Equation (20) as the initialisation of DD.

Figure 7 shows that DD-POD converges faster than DD. As in Figure 8, DD converges slowly—it even takes more than 600 iterations to converge.

For DD-POD, when the number of iteration is 100, the relative errors of potential, current, and power are shown in Table 1. The errors are less than 1%, which means DD-POD converges well. In fact, DD-POD converges so rapidly that it needs only 20 iterations to let the relative error of current achieve the 1%.

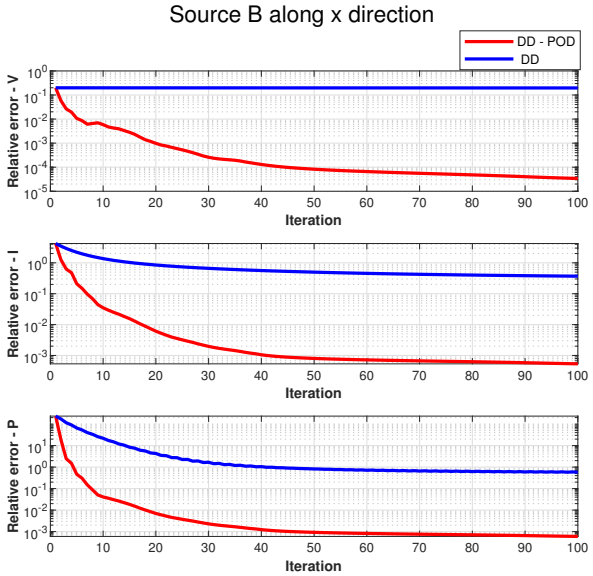

Figure 7. *Cont.*

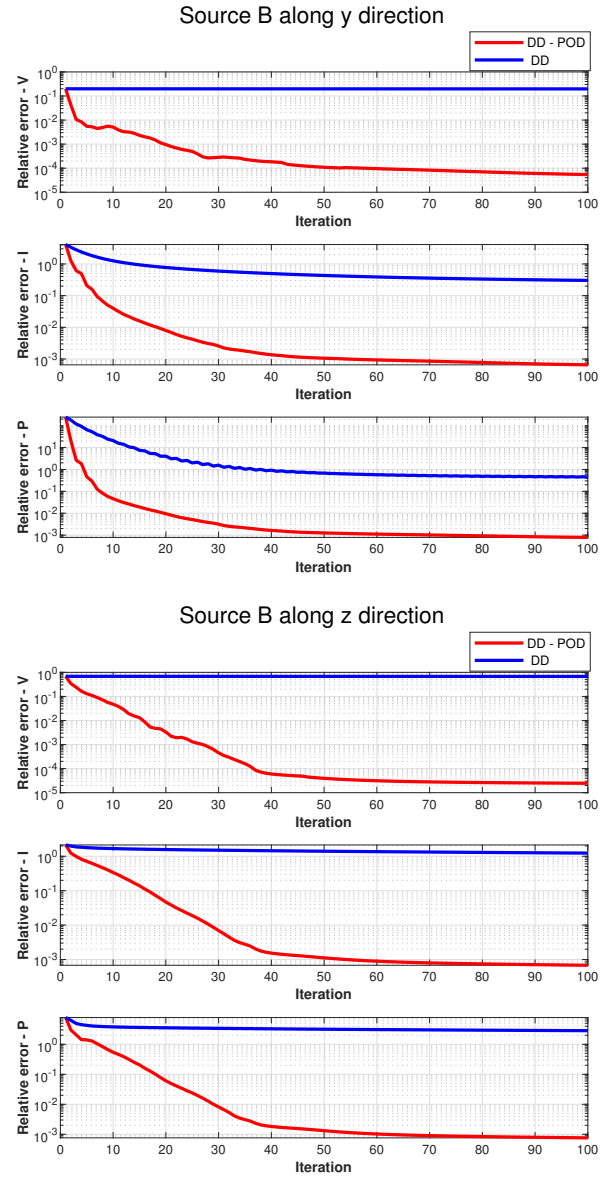

Figure 7. The comparison of convergence between DD and DD-POD.

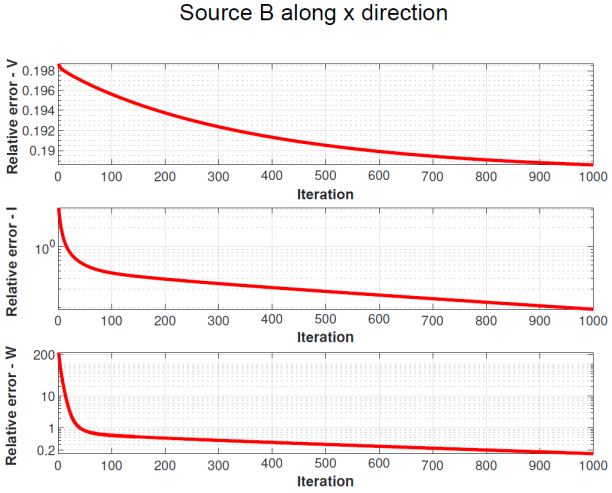

Figure 8. The convergence of DD.

Table 1. Relative error of DD-POD with 100 iterations on the material of size 800 µm × 800 µm × 800 µm divided into 2 × 2 × 2 cells.

Items	B_x Imposed	B_y Imposed	B_z Imposed
Potential	0.003%	0.005%	0.003%
Current	0.054%	0.065%	0.078%
Power	0.060%	0.078%	0.076%

The comparison of potential, current, and power with $\mathbf{B}_x$, $\mathbf{B}_y$, and $\mathbf{B}_z$ imposed, obtained by direct resolution and DD-POD with 100 iterations, is shown in Figures 9 and 10. This result verifies the local accuracy of DD-POD.

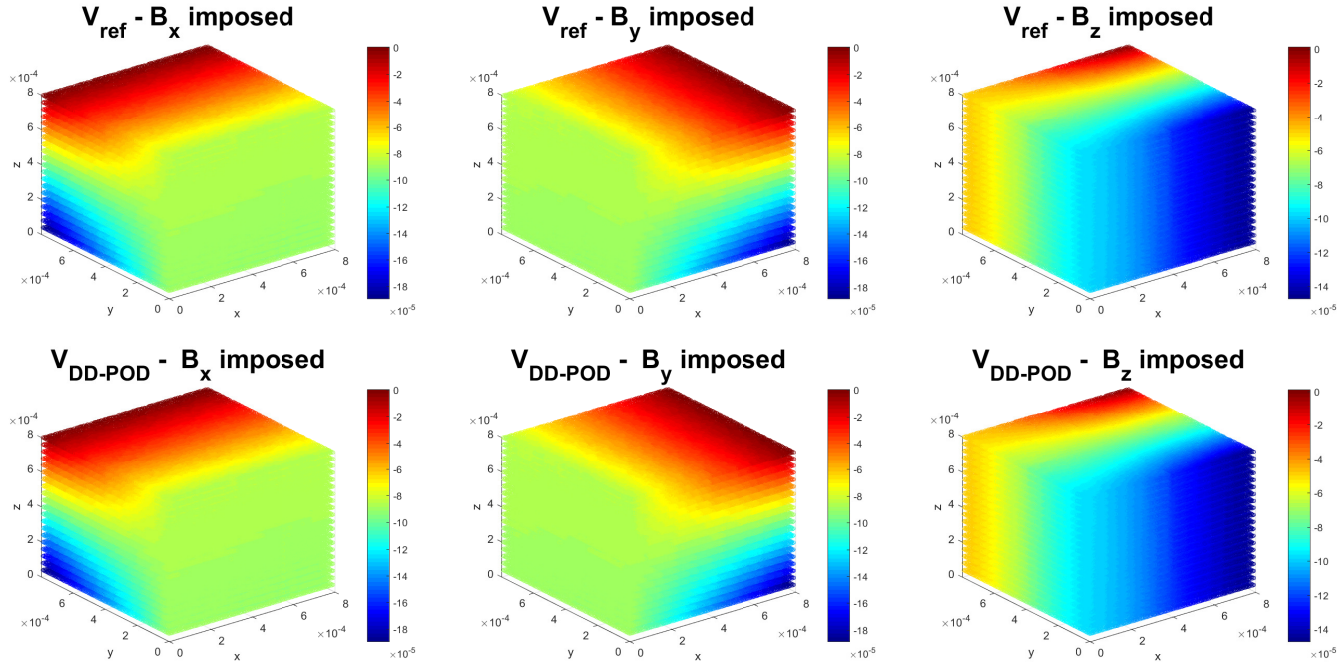

Figure 9. The comparison of potential.

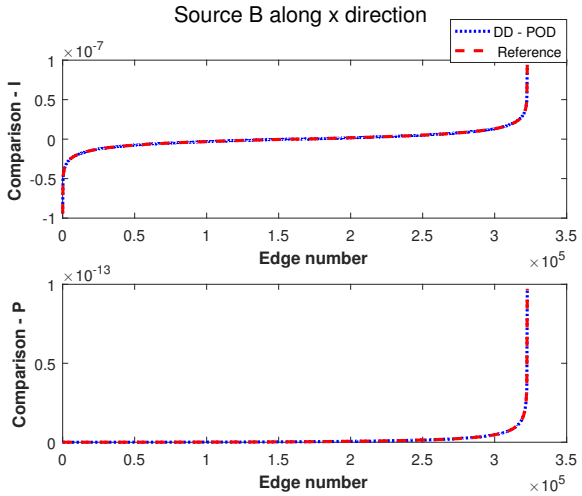

Figure 10. *Cont.*

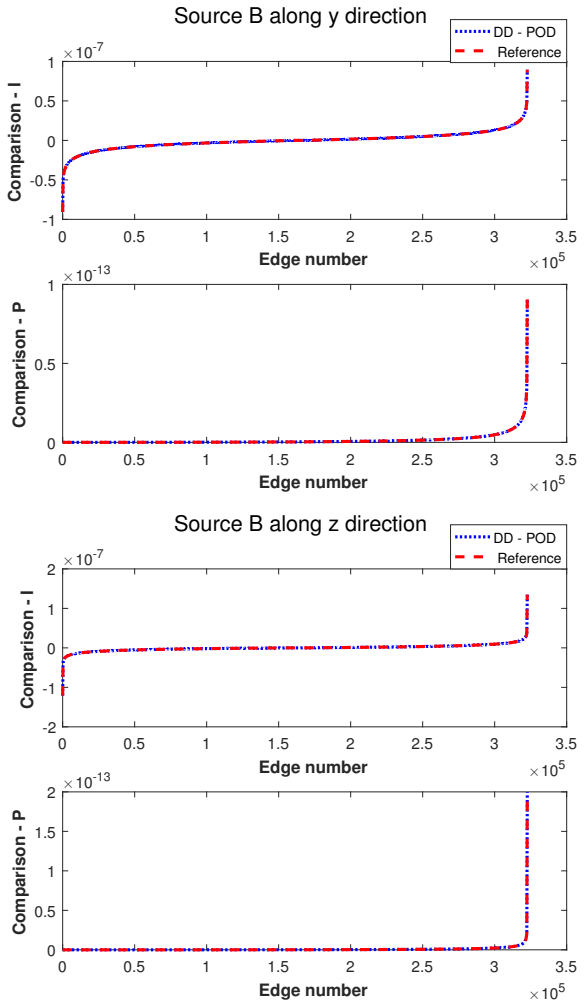

Figure 10. The comparison of sorted current and power.

4.2. Computation Time

As mentioned before, the equation to be solved is an equation with 200,000 unknowns. The resolution direct is conducted by the preconditioned conjugate gradients method with the tolerance set to 10^{-12}. All the times discussed are the CPU time by MATLAB®. The resolution time is defined as the time to solve Equation (11) without considering the time to generate the matrix $\mathbf{K}$ and vector f.

The computation time of direct resolution is 10.07 s, and the computation time of DD (1000 iterations) is 469.78 s, while the computation time of DD-POD is 24.35 s if it stops when the relative error of current reaches 1% (20 iterations), which is much faster than DD.

4.3. Estimation of Parallel Computing Speed-Up

Since DD-POD does not seem to have an improvement in computation time compared with a direct resolution, parallel computing should be introduced.

Currently, the part of code in parallel computing has not been achieved; however, one can simulate the parallel computing time by recording the resolution time in each cell several times and calculating the average. Since there are 2500 nodes in each cell and only a few dozen nodes in contact with neighbouring cells, the exchange of information between cells is neglected in the simulation. The estimated time of parallel computing for the material divided into $2 \times 2 \times 2$ cells with the cell size being 400 µm $\times$ 400 µm $\times$ 400 µm is 6.35 s, which is about 1.6 times faster than a direct solution. When increasing the number of cells, the time of parallel computing does not change significantly when the total number of cells is less than the number of processors if the time needed to exchange information

between processors is not taken into account because the principle of parallel computing is to distribute each task to each processor. When the total number of cells exceeds the number of processors, each processor performs several calculations; therefore, the time required for parallel computing is also proportional to the number of tasks processed by each processor. Figure 11 presents a simulation of parallel computing speed-up.

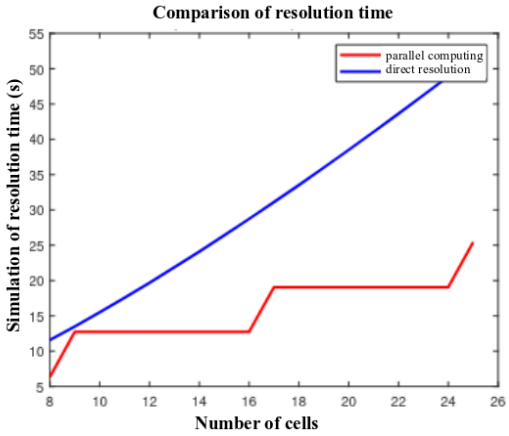

Figure 11. A simulation of parallel computing speed-up.

4.4. Convergence Condition

As in the earlier results, 100 iterations are not necessary; thus, one should propose a new convergence condition to let the resolution stops automatically.

For the convergence condition, one has three choices:

- When the relative error between the potential obtained at iteration i and $i-1$ reaches the tolerance,

$$\varepsilon = \frac{\|V^i - V^{i-1}\|}{\|V^{i-1}\|} < \text{tolerance}; \tag{24}$$

- When the relative error between the current obtained at iteration i and $i-1$ reaches the tolerance,

$$\varepsilon = \frac{\|I^i - I^{i-1}\|}{\|I^{i-1}\|} < \text{tolerance}; \tag{25}$$

- When the relative error between the power obtained at iteration i and $i-1$ reaches the tolerance,

$$\varepsilon = \frac{\|P^i - P^{i-1}\|}{\|P^{i-1}\|} < \text{tolerance}; \tag{26}$$

Since the power is calculated based on the current, the error in the power depends on the error in the current, but calculating the power needs one more calculation step than calculating the current. Therefore, one only compares the effect of the choices of convergence conditions between potential and current. For different choices of convergence condition, the relative errors of potential, current, and power of DD-POD with $\mathbf{B}_x$ imposed are shown in Tables 2 and 3.

Table 2. Relative errors of DD-POD with $\mathbf{B}_x$ imposed for the convergence condition based on potential on the material of size 800 µm × 800 µm × 800 µm divided into 2 × 2 × 2 cells.

Relative Error \ Tolerance	10^{-4}	10^{-5}	10^{-6}
Potential	0.08%	0.01%	0.004%
Current	0.45%	0.12%	0.06%
Power	0.52%	0.14%	0.07%

For the convergence condition based on potential, the resolution stops at the 23rd iteration if the tolerance is defined as 10^{-4}; it stops at the 37th iteration if the tolerance is 10^{-5}; and it stops at the 60th iteration if the tolerance is 10^{-6}.

Table 3. Relative errors of DD-POD with $\mathbf{B}_x$ imposed for the convergence condition based on current on the material of size 800 µm × 800 µm × 800 µm divided into 2 × 2 × 2 cells.

Relative Error \ Tolerance	10^{-4}	10^{-5}
Potential	0.01%	0.004%
Current	0.13%	0.06%
Power	0.14%	0.07%

For the convergence condition based on current, the resolution stops at the 36th iteration if the tolerance is defined as 10^{-4}; it stops at the 63rd iteration if the tolerance is 10^{-5}; and it cannot stop in 100 iterations if the tolerance is 10^{-6}.

For the same tolerance value, the difference between the potentials obtained by two iterations is reached faster than the difference of current. In addition, for the convergence condition based on potential with tolerance defined as 10^{-4}, the relative error is sufficient. With $\mathbf{B}_y$ or $\mathbf{B}_z$ imposed, one has similar results.

Therefore, the convergence condition based on potential with tolerance as 10^{-4} will be used in the following.

4.5. Verification of Convergence

In order to ensure that the convergence of DD-POD is not limited to a certain division of material or a certain position of fibres in material, we have tried to generate other material with random fibres, change the number of cells or size of cells, and thus verify the convergence of DD-POD.

For new material with the same size and same division as the previous material but a different position of fibres, the relative errors of potential, current, and power are shown in Table 4.

Table 4. Relative error of DD-POD on new material of size 800 µm × 800 µm × 800 µm divided into 2 × 2 × 2 cells.

Items	B_x Imposed	B_y Imposed	B_z Imposed
Potential	0.04%	0.05%	0.04%
Current	0.79%	0.84%	0.64%
Power	0.95%	1.03%	0.72%

For material divided into $4 \times 4 \times 4$ cells with the size of cells being 200 µm × 200 µm × 200 µm, the relative errors of potential, current, and power are shown in Table 5.

Table 5. Relative error of DD-POD on new material of size 800 µm × 800 µm × 800 µm divided into 4 × 4 × 4 cells.

Items	B_x Imposed	B_y Imposed	B_z Imposed
Potential	0.03%	0.03%	0.05%
Current	1.28%	0.85%	0.93%
Power	1.55%	1.01%	1.01%

For material with the size 1200 µm × 1200 µm × 1200 µm divided into 3 × 3 × 3 cells, the relative errors of potential, current, and power are shown in Table 6.

The convergence of DD-POD is verified as the relative error does not change significantly with the change of material coupling and parameters of modelling.

Table 6. Relative error of DD-POD on new material of size 1200 µm × 1200 µm × 1200 µm divided into 3 × 3 × 3 cells.

Items	B_x Imposed	B_y Imposed	B_z Imposed
Potential	0.05%	0.04%	0.04%
Current	0.80%	1.05%	1.36%
Power	0.98%	1.25%	1.45%

5. Conclusions and Perspective

Electrical simulation of CFRP at the microscopic scale stays a challenge due to the high number of degrees of freedom and the large domain size required for accurate representativeness. The combination of DD and POD offers a promising alternative to classical homogenisation approaches and allows for keeping local information. However, several improvements are necessary to fully exploit this method.

On the application examples, the relative error calculated by DD-POD is acceptable and the convergence of DD-POD is not limited to a specific geometry. This indicates that DD-POD can be effectively applied to maintain local information in simulations at the microscopic scale, providing a detailed and accurate representation of the material's behaviour. Additionally, the simulation time using DD-POD with parallel computing is faster than direct resolution, as demonstrated in our results. This acceleration is achieved without compromising the accuracy of the simulations, making DD-POD a highly efficient method for conducting electrical simulations of CFRP at the microscopic level.

Future work will focus on incorporating microscopic defects into the simulation cells to further validate and enhance the method's applicability. By introducing these defects, one aims to test the robustness of the DD-POD approach under more complex and realistic conditions. This will not only improve the method's reliability but also extend its usefulness for practical applications in the analysis and design of advanced composite materials.

In conclusion, the integration of DD and POD represents some contribution in the field of computational electromagnetic for CFRP materials. Our study demonstrates that DD-POD can effectively reduce computation time while maintaining accuracy, paving the way for more efficient and detailed simulations. Continued research and development in this area will further enhance the method's capabilities, making it an invaluable tool for engineers and researchers working with composite materials.

Author Contributions: S.L. generated the model of material based on the idea of G.W. and D.T., and performed the computation according to the original idea of A.P., N.B. provided guidance on thermal simulation; S.L. wrote the manuscript with support from all co-authors. All authors have read and agreed to the published version of the manuscript.

Funding: This research is supported by the Pays de la Loire region through WISE program.

Data Availability Statement: The data presented in this study are available on request from the corresponding author. The data are not publicly available due to the fact that the materials are randomly generated each time, the data regarding errors may exhibit slight variations for each newly generated material. Therefore, if necessary, we can provide the source code for material generation to facilitate the verification of errors.

Conflicts of Interest: The authors declare no conflicts of interest.

References

1. Piche, A.; Revel, I.; Peres, G. Experimental and numerical methods to characterize electrical behaviour of carbon fiber composites used in aeronautic industry. In *Advances in Composite Materials-Analysis of Natural and Man-Made Materials*; IntechOpen: London, UK, 2011.
2. Meier, U. Carbon fiber reinforced polymer cables: Why? Why not? What if? *Arab. J. Sci. Eng.* **2012**, *37*, 399–411. [CrossRef]
3. Baechle-Clayton, M.; Loos, E.; Taheri, M.; Taheri, H. Failures and flaws in fused deposition modeling (FDM) additively manufactured polymers and composites. *J. Compos. Sci.* **2022**, *6*, 202. [CrossRef]

4. Gupta, R.; Mitchell, D.; Blanche, J.; Harper, S.; Tang, W.; Pancholi, K.; Baines, L.; Bucknall, D.G.; Flynn, D. A review of sensing technologies for non-destructive evaluation of structural composite materials. *J. Compos. Sci.* **2021**, *5*, 319. [CrossRef]
5. Bui, H.K.; Wasselynck, G.; Trichet, D.; Ramdane, B.; Berthiau, G.; Fouladgar, J. 3-D modeling of thermo inductive non destructive testing method applied to multilayer composite. *IEEE Trans. Magn.* **2013**, *49*, 1949–1952. [CrossRef]
6. Louaayou, M.; Naït-Saïd, N.; Louai, F.Z. 2D finite element method study of the stimulation induction heating in synchronic thermography NDT. *NDT & E Int.* **2008**, *41*, 577–581.
7. Netzelmann, U.; Walle, G.; Lugin, S.; Ehlen, A.; Bessert, S.; Valeske, B. Induction thermography: Principle, applications and first steps towards standardisation. *Quant. Infrared Thermogr. J.* **2016**, *13*, 170–181. [CrossRef]
8. Bui, H.K. Contribution à la Modélisation Multiphysique des Matériaux Composites Stratifié: Application au CND Thermo-Inductifs. Ph.D. Thesis, Nantes University, Nantes, France, 2014.
9. Wasselynck, G. Etude des Interactions entre les Ondes Électromagnétiques de Fréquences Moyennes et les Matériaux Composites: Application à L'assemblage par Induction de ces Matériaux. Ph.D. Thesis, Nantes University, Nantes, France, 2011.
10. Senghor, F.D.; Wasselynck, G.; Bui, H.K.; Branchu, S.; Trichet, D.; Berthiau, G. Electrical conductivity tensor modeling of stratified woven-fabric carbon fiber reinforced polymer composite materials. *IEEE Trans. Magn.* **2017**, *53*. [CrossRef]
11. Kane, B.; Pierquin, A.; Wasselynck, G.; Trichet, D. Coupled Numerical and Experimental Identification of Geometrical Parameters for Predicting the Electrical Conductivity of CFRP Layers. *IEEE Trans. Magn.* **2020**, *56*, 6701604. [CrossRef]
12. Wasselynck, G.; Trichet, D.; Fouladgar, J. Determination of the electrical conductivity tensor of a CFRP composite using a 3-D percolation model. *IEEE Trans. Magn.* **2013**, *49*, 1825–1828. [CrossRef]
13. Blech, C.; Sreekumar, H.K.; Hüpel, Y.; Langer, S.C. Efficient solution strategies for cabin noise assessment of a wave resolving aircraft fuselage model. *arXiv* **2023**, arXiv:2310.04734.
14. Chinesta, F.; Ammar, A.; Cueto, E. Recent advances and new challenges in the use of the proper generalized decomposition for solving multidimensional models. *Arch. Comput. Methods Eng.* **2010**, *17*, 327–350. [CrossRef]
15. Henneron, T.; Benabou, A.; Clenet, S. Nonlinear proper generalized decomposition method applied to the magnetic simulation of a SMC microstructure. *IEEE Trans. Magn.* **2012**, *48*, 3242–3245. [CrossRef]
16. Henneron, T.; Clenet, S. Model-order reduction of multiple-input non-linear systems based on POD and DEI methods. *IEEE Trans. Magn.* **2015**, *51*, 7207104. [CrossRef]
17. Burgard, S.; Farle, O.; Loew, P.; Dyczij-Edlinger, R. Fast shape optimization of microwave devices based on parametric reduced-order models. *IEEE Trans. Magn.* **2014**, *50*, 629–632. [CrossRef]
18. Schmidthäusler, D.; Schöps, S.; Clemens, M. Reduction of linear subdomains for non-linear electro-quasistatic field simulations. *IEEE Trans. Magn.* **2013**, *49*, 1669–1672. [CrossRef]
19. Krauklis, A.E.; Karl, C.W.; Rocha, I.B.C.M.; Burlakovs, J.; Ozola-Davidane, R.; Gagani, A.I.; Starkova, O. Modelling of Environmental Ageing of Polymers and Polymer Composites—Modular and Multiscale Methods. *Polymers* **2022**, *14*, 216. [CrossRef] [PubMed]
20. Lopez, E.; Gonzalez, D.; Aguado, J.; Abisset-Chavanne, E.; Cueto, E.; Binetruy, C.; Chinesta, F. A manifold learning approach for integrated computational materials engineering. *Arch. Comput. Methods Eng.* **2018**, *25*, 59–68. [CrossRef]
21. El-Ghamrawy, K.; Zlotnik, S.; Auricchio, F.; Díez, P. Proper generalized decomposition solutions for composite laminates parametrized with fibre orientations. *Comput. Mech.* **2023**, *71*, 89–105. [CrossRef]
22. Corigliano, A.; Dossi, M.; Mariani, S. Model order reduction and domain decomposition strategies for the solution of the dynamic elastic–plastic structural problem. *Comput. Methods Appl. Mech. Eng.* **2015**, *290*, 127–155. [CrossRef]
23. Radermacher, A.; Reese, S. Model reduction in elastoplasticity: Proper orthogonal decomposition combined with adaptive sub-structuring. *Comput. Mech.* **2014**, *54*, 677–687. [CrossRef]
24. Ponnamma, D.; Ninan, N.; Thomas, S. Carbon nanotube tube filled polymer nanocomposites and their applications in tissue engineering. In *Applications of Nanomaterials*; Elsevier: Amsterdam, The Netherlands, 2018; pp. 391–414.
25. Toselli, A.; Widlund, O. *Domain Decomposition Methods-Algorithms and Theory*; Springer Science & Business Media: Berlin/Heidelberg, Germany, 2004; Volume 34.
26. Holst, M. *Algebraic Schwarz Theory*; Technical Report CRPC-94–12 Applied Mathematics and CRPC; Center for Research on Parallel Computation: Houston, TX, USA, 1994.
27. Luo, Z.; Chen, G. *Proper Orthogonal Decomposition Methods for Partial Differential Equations*; Academic Press: Cambridge, MA, USA, 2018.
28. Baranger, J.; Arnal, B.; Perren, F.; Baud, O.; Tanter, M.; Demené, C. Adaptive spatiotemporal SVD clutter filtering for ultrafast Doppler imaging using similarity of spatial singular vectors. *IEEE Trans. Med. Imaging* **2018**, *37*, 1574–1586. [CrossRef] [PubMed]